Optimized Detection of Exogenous Contrast Agents Using Two-Wavelength Photoacoustic Imaging

Franco Castro
School of Electrical Engineering
Universidad de Costa Rica
San José, Costa Rica
franco.castro@ucr.ac.cr

Diego S. Dumani
School of Electrical Engineering
Universidad de Costa Rica
San José, Costa Rica
diego.dumani@ucr.ac.cr

***Abstract*—The detection of gold nanoparticles (AuNPs) is critical in photoacoustic imaging due to their potential applications in biomedical research and cancer detection. This paper compares two methods for detecting AuNPs in simulated environments: the Least Squares Method and the Direct-Inverse Product Method, the latter developed by the authors. Simulations were conducted using MATLAB, considering three chromophores: oxyhemoglobin, deoxyhemoglobin, and AuNPs as the contrast agent. Results demonstrate that the Direct-Inverse Product Method requires fewer wavelengths (two) compared to the Least Squares Method (at least $N+1$), achieving similar or better detection accuracy under specific conditions. The highest correlation of 0.8077 was obtained with radially decreasing AuNP concentrations in regions with varying oxyhemoglobin and deoxyhemoglobin concentrations. This study highlights the strengths and limitations of both methods, emphasizing the trade-offs between computational simplicity and detection robustness.**

***Index Terms*—photoacoustic imaging, exogenous contrast agents, gold nanoparticles, cancer, biomedical imaging**

I. Introduction

Biomedical imaging allows the visualization of structures and biological processes within a body. These images play a critical role in diagnosing, treating, and monitoring various medical conditions in organisms. Common methods of medical imaging include computed tomography, magnetic resonance imaging, ultrasound, and the technique central to this paper: photoacoustic imaging [1]–[4].

Combining light and sound, photoacoustic imaging creates detailed visuals of internal structures. A pulsed laser targets a tissue, and as the light is absorbed, the tissue heats and emits sound waves. Captured by transducers, these waves are transformed into images that display the internal structure of the body based on the optical absorption properties of the tissue's molecules [5]–[7]. This technique has proven effective in a variety of applications such as tumor detection, brain vascular imaging, imaging blood vessels, quantifying oxygen saturation, identifying melanoma, and detecting lipids in vessels [5].

In order to facilitate the visualization of specific processes or structures within the body, an exogenous agent can be introduced. In photoacoustic imaging, an exogenous contrast agent is a substance that absorbs light strongly at specific wavelengths, thereby enhancing the delineation and contrast of areas of interest within the images [5]. For instance, gold nanoparticles can adhere to different types of cells upon injection. Detecting cancer cells within a biomedical image can be challenging; however, the use of gold nanoparticles with suitable optical properties can significantly improve the detection of these cells. Subsequently, an algorithm that uses photoacoustic images with different wavelengths can be developed to detect the gold nanoparticles, thereby aiding in the precise localization of cancer cells or immune cells (see Fig. 1) [8].

In general, a photoacoustic image differs from another if different wavelengths are used in their formation, as the contrast of each image depends on the specific wavelength employed. This is because the optical absorption of chromophores[1] varies across the electromagnetic spectrum. Based on this principle, several studies have developed methods that utilize multiple photoacoustic images to detect contrast agents [8]–[10]. These methods take advantage of the distinct optical absorption properties of chromophores, thereby enhancing the diagnostic capabilities of the imaging.

The purpose of this article is to present a new method for detecting exogenous contrast agents, optimizing photoacoustic imaging resources by utilizing only two wavelengths. As a performance metric, the developed method will be compared to the least squares method, which is the most commonly used in the references consulted for drafting this article, using the image correlation.

II. Methodology

A. Photoacoustic Imaging

When the photoacoustic effect is induced such that the laser energy distribution is uniform throughout the tissue, the initial acoustic pressure in the tissue, denoted as p_0 in Pa, is given by the following expression [4], [11]:

$$p_0(\mathbf{r},\lambda) = \Gamma \mu_a(\mathbf{r},\lambda) F(\lambda) \tag{1}$$

[1]In photoacoustics, a chromophore is defined as a substance that absorbs light. The absorption of light by the chromophore results in the conversion of optical energy into thermal energy. Chromophores may be endogenous, such as blood, water, lipids, and melanin, or exogenous, serving as contrast agents. [4], [9]

The initial pressure distribution p_0 is influenced by three key factors: the thermoacoustic conversion efficiency, also known as the Grüneisen parameter Γ (dimensionless), the local optical absorption coefficient $\mu_a(\mathbf{r}, \lambda)$ in m^{-1}, and the optical laser fluence $F(\lambda)$ in $\mathrm{J/m}^2$.

Note that both the initial pressure p_0 and the local optical absorption coefficient μ_a are dependent on the position $\mathbf{r}$, as they represent a distribution of magnitudes. This means their values depend on the specific point within the tissue where they are measured. Similarly, the local optical absorption coefficient μ_a and the fluence F are wavelength-dependent (λ) because the optical absorption of the chromophores in the tissue varies across the electromagnetic spectrum and the energy output from two different lasers does not necessarily have to be the same.

Given chromophores $1, \ldots, n, \ldots, N$, the optical absorption of the n-th chromophore is directly proportional to its local concentration $C_n(\mathbf{r})$ in $\mathrm{mol/m}^3$ and its specific absorption coefficient spectra $\varepsilon_n(\lambda)$ in $\mathrm{m}^2/\mathrm{mol}$. Therefore, the local optical absorption coefficient corresponds to the sum of the individual optical absorptions of each chromophore [9]:

$$\mu_a(\mathbf{r}, \lambda) = \sum_{n}^{N} C_n(\mathbf{r}) \varepsilon_n(\lambda) \tag{2}$$

B. Detection of chromophores

Let m be the chromophore we want to detect; the method for its detection is based on defining an equation as follows:

$$\Xi_m(\mathbf{r}) = \begin{cases} 1 \iff \text{The concentration of } m \text{ is non zero} \\ 0 \iff \text{The concentration of } m \text{ is zero.} \end{cases} \tag{3}$$

In this equation, the term $\Xi_m(\mathbf{r})$ denotes an image that shows a distribution of all points containing a non-zero concentration of the chromophore m of interest by assigning a value of 1 to those pixels.

Considering a real example, Fig. 1 illustrates the contrast between gold nanoparticles (AuNP) adhering to cancer cells traveling through a blood vessel and the capability of image $\Xi_{\mathrm{AuNP}}(\mathbf{r})$ to detect cancer by locating these nanoparticles.

The approach to approximating the image $\Xi_m(\mathbf{r})$ is not unique. In this article, we will use two methods: one already existing in the literature, the least squares method, and the other developed by the authors, which we will refer to as the direct-inverse product method.

C. Least squares method

The least squares method starts from having more equations than variables, which means more images than chromophores. That is, if we have I images and N chromophores, then $I > N$. This condition is fundamental for applying the least squares method.

If we group the I measured photoacoustic images into a vector $\mathbf{p}$ as follows:

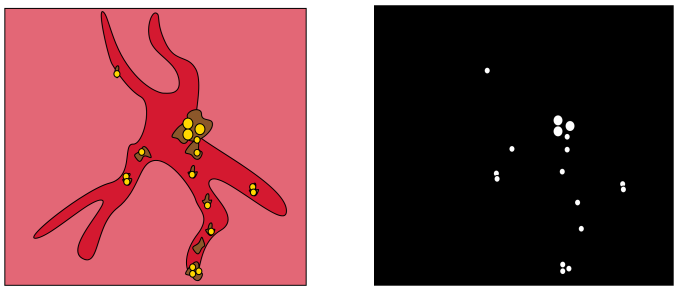

(a) Reality (b) $\Xi_{\mathrm{AuNP}}(\mathbf{r})$

Fig. 1: (a) Gold nanoparticles (AuNP) adhering to cancer cells in a blood vessel. (b) Image showing the location of the cancer cells by detecting the gold nanoparticles.

$$\mathbf{p}(\mathbf{r}) = \begin{pmatrix} p_1(\mathbf{r}, \lambda_1) \\ \vdots \\ p_i(\mathbf{r}, \lambda_i) \\ \vdots \\ p_I(\mathbf{r}, \lambda_I) \end{pmatrix} \tag{4}$$

We can define the i-th photoacoustic image as:

$$\underbrace{p_i(\mathbf{r}, \lambda_i)}_{\text{measurement}} = \underbrace{\Gamma C(\mathbf{r}) \varepsilon(\lambda_i) F(\lambda_i) + e_i}_{\text{photoacoustic image model with associated measurement error}} \tag{5}$$

In (5), an error e_i is assigned to each photoacoustic image. This error is arbitrary and allows the concentration matrix $C_m(\mathrm{r})$ of interest to be algebraically solved using the procedure shown below. If the following matrices are defined:

$$\mathbf{A} = \begin{pmatrix} \Gamma\varepsilon_1(\lambda_1)F(\lambda_1) & \cdots & \Gamma\varepsilon_n(\lambda_1)F(\lambda_1) & \cdots & \Gamma\varepsilon_N(\lambda_1)F(\lambda_1) \\ \vdots & \ddots & \vdots & \ddots & \vdots \\ \Gamma\varepsilon_1(\lambda_i)F(\lambda_i) & \cdots & \Gamma\varepsilon_n(\lambda_i)F(\lambda_i) & \cdots & \Gamma\varepsilon_N(\lambda_i)F(\lambda_i) \\ \vdots & \ddots & \vdots & \ddots & \vdots \\ \Gamma\varepsilon_1(\lambda_I)F(\lambda_I) & \cdots & \Gamma\varepsilon_n(\lambda_I)F(\lambda_I) & \cdots & \Gamma\varepsilon_N(\lambda_I)F(\lambda_I) \end{pmatrix} \tag{6}$$

$$\mathbf{C} = \begin{pmatrix} C_1(\mathbf{r}) \\ \vdots \\ C_n(\mathbf{r}) \\ \vdots \\ C_N(\mathbf{r}) \end{pmatrix} \tag{7}$$

$$\mathbf{e} = \begin{pmatrix} e_1 \\ \vdots \\ e_n \\ \vdots \\ e_N \end{pmatrix} \tag{8}$$

It is possible to formulate the following system of equations:

$$\mathbf{p}(\mathbf{r}) = \mathbf{AC} + \mathbf{e} \tag{9}$$

The least squares method, as its name suggests, involves taking the squared Euclidean norm of the error vector e, which we will denote as S,

$$S = \|\mathbf{p} - \mathbf{AC}\|^2 = \sum_{i=1}^{I} {e_i}^2 \tag{10}$$

and minimizes this value S by taking its matrix derivative with respect to $\mathbf{C}$.

$$\frac{\partial S}{\partial \mathbf{C}} = 0 \tag{11}$$

To find $\mathbf{C}$, note that the squared norm is expanded as:

$$S = (\mathbf{p} - \mathbf{AC})^\top (\mathbf{p} - \mathbf{AC}) \tag{12}$$

Expanding this product:

$$S = \mathbf{p}^\top \mathbf{p} - 2\mathbf{p}^\top A\mathbf{C} + \mathbf{C}^\top \mathbf{A}^\top \mathbf{AC} \tag{13}$$

The partial derivative of S with respect to $\mathbf{C}$ (using matrix differentiation rules) is:

$$\frac{\partial S}{\partial \mathbf{C}} = -2\mathbf{A}^\top \mathbf{p} + 2\mathbf{A}^\top \mathbf{AC} \tag{14}$$

To minimize S, we equate the derivative to zero, eliminate the factor 2 (as it does not affect the solution), and reorganize:

$$\mathbf{A}^\top \mathbf{p} + \mathbf{A}^\top \mathbf{AC} = 0 \tag{15}$$

Solving for $\mathbf{C}$, the solution is:

$$\mathbf{C} = (\mathbf{A}^\top \mathbf{A})^{-1} \mathbf{A}^\top \mathbf{p} \tag{16}$$

Let m be our chromophore of interest. If we extract $C_m(\mathbf{r})$ from $\mathbf{C}$, then we can define our matrix detection (3) as:

$$\Xi_m(\mathbf{r}) = \begin{cases} 1 \iff C_m(\mathbf{r}) \neq 0 \\ 0 \iff C_m(\mathbf{r}) = 0 \end{cases} \tag{17}$$

Finally, note that applying this method fundamentally requires knowledge of all the parameters in the matrix $\mathbf{A}$, as it involves the operator $(\mathbf{A}^\top \mathbf{A})^{-1}\mathbf{A}^\top$, which is applied to the measured images $\mathbf{p}$.

Therefore, the Grüeneisen coefficient Γ, the fluence $F(\lambda_i)$, and the molar absorption coefficients must be well known at the different wavelengths $\lambda_1, \cdots, \lambda_i, \cdots, \lambda_I$.

D. Direct-inverse product method

The direct-inverse product method consists of a way to approximate the detection image (3) independently of the chromophores present in the tissue, using only two wavelengths. These wavelengths are selected within a region where the geometry of the molar absorption curves $(\varepsilon_1(\lambda), \cdots, \varepsilon_n(\lambda), \cdots, \varepsilon_N(\lambda))$ is appropriate.

The method starts by multiplying photoacoustic images directly and inversely, as expressed in the following equation:

$$\xi_m(\mathbf{r}) = \prod_{k=1}^{K} \frac{p_0(\mathbf{r}, \lambda^k)}{p_0(\mathbf{r}, \lambda_k)} \tag{18}$$

In this equation, K is a free parameter defined as the number of iterations needed to approximate $\Xi_m(\mathbf{r})$. This term is closely related to another free parameter called the threshold T, whose relationship will be discussed after defining all the symbols in (18).

The superscript k in the variable λ^k does not represent a power or any similar operation. Both λ^k and λ_k are wavelengths that satisfy geometric properties, which are detailed below:

Given the presence of chromophores $1, \ldots, n \ldots, N$ during the detection of the contrast agent m, the following must be satisfied:

- We define a wavelength as being of the form λ^k if it lies within a region of the electromagnetic spectrum where the specific absorption coefficient of the contrast agent m is greater than the specific absorption coefficients of the remaining N chromophores. Specifically,

$$\varepsilon_m(\lambda^k) > \varepsilon_n(\lambda^k), \quad n = 1, \ldots, N \tag{19}$$

- We define a wavelength as being of the form λ_k if it lies within a region of the electromagnetic spectrum where the specific absorption coefficient of the contrast agent m is less than the specific absorption coefficients of the remaining N chromophores. Specifically,

$$\varepsilon_m(\lambda_k) < \varepsilon_n(\lambda_k), \quad n = 1, \ldots, N \tag{20}$$

A set of specific absorption coefficients that satisfy (19) and (20) can be visualized in Fig. 2. The red area contains all the wavelengths of the form λ^k, and the blue area contains all the wavelengths of the form λ_k.

Once all the terms have been defined, to understand how to approximate $\Xi(\mathbf{r})$ from $\xi(\mathbf{r})$, we consider two distinct points, $\mathbf{r_1}$ and $\mathbf{r_2}$, in space. The difference lies in the fact that $\mathbf{r_1}$ contains gold, while $\mathbf{r_2}$ does not. Specifically:

$$\begin{cases} C_m(\mathbf{r}_1) \neq 0 \wedge C_n(\mathbf{r}_1) \neq 0, \\ C_m(\mathbf{r}_2) = 0 \wedge C_n(\mathbf{r}_2) \neq 0 \end{cases} \tag{21}$$

Now, we will evaluate the points $\mathbf{r}_1$ and $\mathbf{r}_2$ in $\xi_m(\mathbf{r})$ to proof how the detection of the chromophore m works. If we substitute (1) into (18), we obtain:

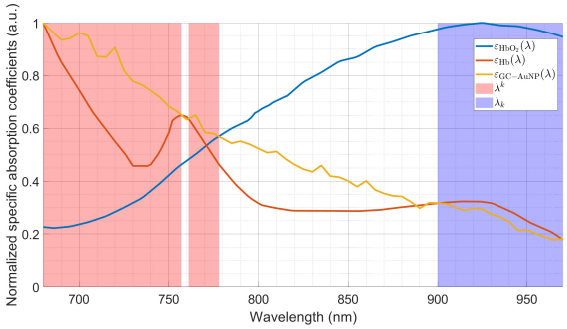

Fig. 2: Specific absorption coefficients of gold nanoparticles as a contrast agent, and (AuNP), oxyhemoglobin (HbO_2) and deoxyhemoglobin (HbO)

$$\xi_m(\mathbf{r}) = \prod_{k=1}^{K} \frac{\not{F}F(\lambda^k)\mu_a(\mathbf{r},\lambda^k)}{\not{F}F(\lambda_k)\mu_a(\mathbf{r},\lambda_k)} \tag{22}$$

If we express the local optical absorption coefficients as the sum of the individual contributions from the absorption of the contrast agent m and the N remaining chromophores according to (2), the result is:

$$\frac{\mu_a(\mathbf{r},\lambda^k)}{\mu_a(\mathbf{r},\lambda_k)} = \frac{C_m(\mathbf{r})\varepsilon_m(\lambda^k) + \sum_{n=1}^{N} C_n(\mathbf{r})\varepsilon_n(\lambda^k)}{C_m(\mathbf{r})\varepsilon_m(\lambda_k) + \sum_{n=1}^{N} C_n(\mathbf{r})\varepsilon_n(\lambda_k)} \tag{23}$$

The inequality (19) implies that, since $\varepsilon(\lambda^k)$ and $\varepsilon(\lambda_k)$ are positive real numbers, for each λ^k there exists a real number $\sigma^n(\lambda^k) > 1$ such that:

$$\varepsilon_n(\lambda^k) = \frac{\varepsilon_m(\lambda^k)}{\sigma^n(\lambda^k)} \tag{24}$$

Similarly, let $\sigma_n(\lambda_k) > 1$. Then, for each λ_k, the following holds:

$$\varepsilon_n(\lambda_k) = \varepsilon_m(\lambda_k)\sigma_n(\lambda_k) \tag{25}$$

Substituting (24) and (25) into (23) and factoring $\varepsilon_m(\lambda^k)$ and $\varepsilon_m(\lambda_k)$, the result is:

$$\frac{\mu_a(\mathbf{r},\lambda^k)}{\mu_a(\mathbf{r},\lambda_k)} = \frac{\varepsilon_m(\lambda^k)}{\varepsilon_m(\lambda_k)} \frac{C_m(\mathbf{r}) + \sum_{n=1}^{N} \frac{C_n(\mathbf{r})}{\sigma^n(\lambda^k)}}{C_m(\mathbf{r}) + \sum_{n=1}^{N} C_n(\mathbf{r})\sigma_n(\lambda_k)} \tag{26}$$

Now, substituting (26) into (22), we obtain:

$$\xi_m(\mathbf{r}) = \prod_{k=1}^{K} \underbrace{\frac{F(\lambda^k)}{F(\lambda_k)} \frac{\varepsilon_m(\lambda^k)}{\varepsilon_m(\lambda_k)}}_{A_k} \underbrace{\frac{C_m(\mathbf{r}) + \sum_{n=1}^{N} \frac{C_n(\mathbf{r})}{\sigma^n(\lambda^k)}}{C_m(\mathbf{r}) + \sum_{n=1}^{N} C_n(\mathbf{r})\sigma_n(\lambda_k)}}_{B_k(\mathbf{r})} \tag{27}$$

Now, assuming we are in a region where the N irrelevant chromophores are uniformly distributed, i.e., $C_n(\mathbf{r}_1) = C_n(\mathbf{r}_2)$, it follows that:

$$B_k(\mathbf{r}_1) > B_k(\mathbf{r}_2) \tag{28}$$

$$A_k B_k(\mathbf{r}_1) > A_k B_k(\mathbf{r}_2) \tag{29}$$

$$\prod_{k=1}^{K} A_k B_k(\mathbf{r}_1) > \prod_{k=1}^{K} A_k B_k(\mathbf{r}_2) \tag{30}$$

$$\xi(\mathbf{r}_1) > \xi(\mathbf{r}_2) \tag{31}$$

Therefore, if we choose a threshold T such that:

$$\xi(\mathbf{r}_1) > T > \xi(\mathbf{r}_2) \tag{32}$$

We obtain the following approximation for (18) using photoacoustic images:

$$\Xi_m(\mathbf{r}) \approx \begin{cases} 1 \iff \xi(\mathbf{r}) > T \\ 0 \iff \xi(\mathbf{r}) < T \end{cases} \tag{33}$$

We describe (33) as an approximation because we cannot guarantee that irrelevant chromophores are uniformly distributed. For instance, the distribution of hemoglobin varies significantly depending on the quantity and organization of blood vessels in specific tissue [12], [13]. However, it is possible to limit the analysis of a biomedical image to a tissue region where the distribution is approximately constant.

Furthermore, it is important to mention that the detection quality of the contrast agent m is directly related to the adjustment of the parameters K and T. Testing different combinations can lead to more efficient detection. In the results section, a comparison is made between two images formed using different combinations of K and T to illustrate the improvement of one over the other.

III. Results and Discussion

A. Testing the Direct-Inverse Product Method

To verify the functionality of the method, three simulations were conducted in MATLAB, as shown in Fig. 3, Fig. 4, and Fig. 5. In all simulations, three chromophores were considered: 1) oxyhemoglobin (HbO_2), 2) deoxyhemoglobin (Hb), and 3) gold nanoparticles (AuNP) as the contrast agent. The objective is to simulate an environment similar to that of cancer cell detection by identifying gold nanoparticles, as described in [8].

To generate the images shown in the figures, simulations were conducted using the parameters listed in Table I. For each chromophore's concentration, an NxM grid was created with random values within the intervals specified in the table. The absorption coefficients for each chromophore were derived from the normalized data used to construct Fig. 2. In all simulations, the Grüneisen coefficient and laser fluence were held constant to ensure that the analysis focused solely on the optical absorption properties of the chromophores.

In the figures, image (a) represents the actual concentration of gold nanoparticles. Images (b) and (c) show the results

TABLE I: Numerical values used in simulations

Parameter	Sim. Fig. 3	Sim. Fig. 4	Sim. Fig. 5
Grid ($N \times M$)		1000×1000	
C_{AuNP}	$[0, 25]$	$[0, 75]$	
$C_{\mathrm{Hb0_2}}$		$[0, 100]$	$[0, 400]$
C_{Hb0}		$[0, 100]$	$[0, 400]$
λ^k		720nm	
λ_k		930nm	
$\varepsilon_{\mathrm{AuNP}}(\lambda^k)$		0.906875	
$\varepsilon_{\mathrm{AuNP}}(\lambda_k)$		0.275261	
$\varepsilon_{\mathrm{AuNP}}(880\mathrm{nm})$		0.341918395	
$\varepsilon_{\mathrm{Hb0_2}}(\lambda^k)$		0.283572	
$\varepsilon_{\mathrm{Hb0_2}}(\lambda_k)$		0.31722	
$\varepsilon_{\mathrm{Hb0_2}}(880\mathrm{nm})$		0.940352021	
$\varepsilon_{\mathrm{Hb}}(\lambda^k)$		0.550633	
$\varepsilon_{\mathrm{Hb}}(\lambda_k)$		0.995763	
$\varepsilon_{\mathrm{Hb}}(880\mathrm{nm})$		0.301687764	
Γ		0.1	
F		100	
K		5 and 10	
T		0.75 and 0.04	

Note: In the third simulation in Fig. 5, $\mathrm{Hb0_2}$ and Hb concentrations vary within the range [0,400] but are not uniformly distributed. The grid is divided into four 500 × 500 submatrices, each containing concentrations in the intervals $[0, 100]$, $[100, 200]$, $[200, 300]$, and $[300, 400]$, arranged counterclockwise.

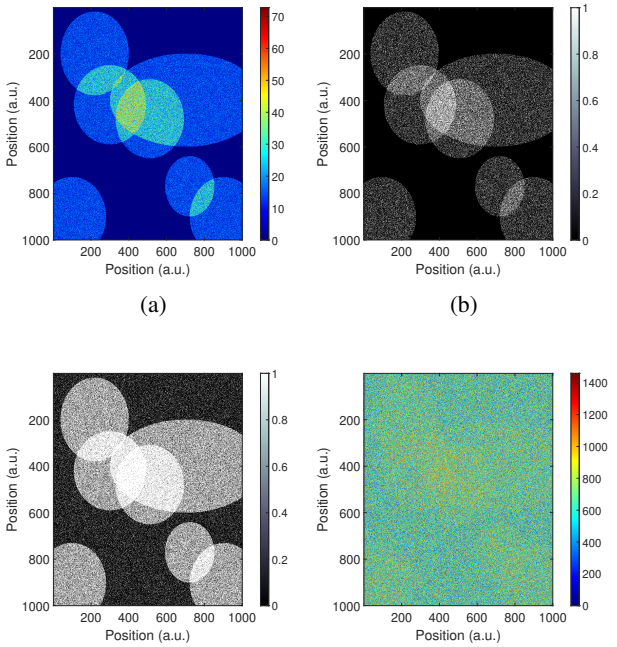

Fig. 3: Detection of elliptical masked regions containing concentrations of gold nanoparticles. (a) Concentration of gold nanoparticles, $C_{\mathrm{AuNP}}(\mathbf{r})$. (b) Detection of gold nanoparticles, $\Xi_{\mathrm{AuNP}}(\mathbf{r})$, with $K = 5$ and $T = 0.75$. (c) Detection of gold nanoparticles, $\Xi_{\mathrm{AuNP}}(\mathbf{r})$, with $K = 10$ and $T = 0.04$. (d) Photoacoustic image at $880\mathrm{nm}$, $p_0(\mathbf{r}, 880\mathrm{nm})$.

of applying the contrast agent detection method to locate the gold nanoparticles. The difference between them is that for (b), the iterations were set to $K = 5$ with a threshold of $T = 0.75$, while for (c), the number of iterations was increased to $K = 10$ and the threshold was lowered to $T = 0.04$. These images aim to demonstrate that the quality of gold nanoparticle detection is directly influenced by the adjustment of the parameters K and T. In this case, more iterations with a lower threshold result in more efficient detection of the contrast agent, albeit with the drawback of some false positives. Finally, image (d) corresponds to a photoacoustic image taken at $880\mathrm{nm}$, intended to illustrate that a photoacoustic image without wavelength-specific criteria is not effective for contrast agent detection

The simulation depicted in Fig. 3 aims to demonstrate the method's capability to detect regions with AuNP concentrations. Elliptical masks with random distributions of the contrast agent were created for this purpose. The figure illustrates that the detection method successfully identifies areas with higher concentrations of AuNP, resulting in brighter contrasts in regions containing the contrast agent, and darker contrasts in areas without it.

To assess the method's limitations, the simulation depicted in Fig. 4 was conducted. In this simulation, a highly concentrated AuNP region was created at the center of the grid, with the concentration of the contrast agent decreasing radially. The results indicate that the detection method becomes less effective as the concentration of the contrast agent decreases relative to the concentration of other non-target chromophores. Therefore, to ensure optimal performance of the method, it is crucial to maintain a sufficient concentration of the contrast agent.

To further challenge the method and gain a clearer understanding of the impact of varying the parameters K and T, the simulation depicted in Fig. 5 was conducted. In this scenario, the concentrations of $\mathrm{HbO_2}$ and Hb were not uniformly distributed across the tissue. Instead, the mesh was divided into four equal sections. As the regions are traversed counterclockwise, the concentration of non-target chromophores gradually increases. This setup allows for two critical observations: First, as the concentration of blood components increases, the method's effectiveness in detecting regions with low AuNP concentrations diminishes. Second, increasing the number of iterations K and appropriately adjusting the threshold T significantly enhances the method's detection capability. However, it is important to mention that in a real experiment, it should be considered that gold nanoparticles are an excellent contrast agent because, for the same volume element, pure gold is capable of generating a concentration up to 6300 times greater than that of hemoglobin (see Appendix B).

Finally, it is important to note that the primary limitation of these results is that the method's effectiveness has been validated only through simulations. The potential impact of real-world factors, such as acoustic and electronic noise, as well as light scattering and attenuation, remains uncertain when applying the photoacoustic image multiplication as described in (18).

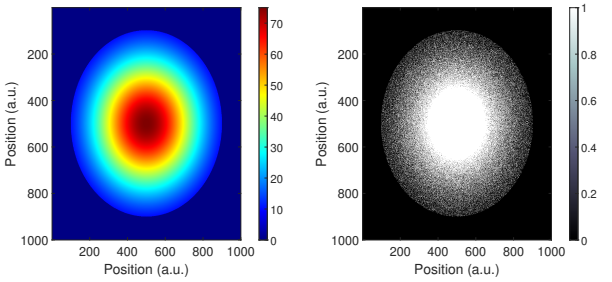

(a) (b)

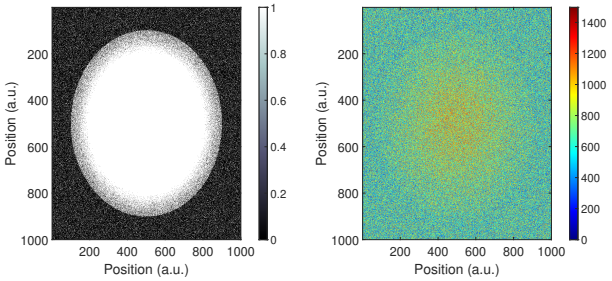

(c) (d)

Fig. 4: Detection of radially decreasing gold nanoparticles. (a) Concentration of gold nanoparticles, $C_{\mathrm{AuNP}}(\mathbf{r})$. (b) Detection of gold nanoparticles, $\Xi_{\mathrm{AuNP}}(\mathbf{r})$, with $K = 5$ and $T = 0.75$. (c) Detection of gold nanoparticles, $\Xi_{\mathrm{AuNP}}(\mathbf{r})$, with $K = 10$ and $T = 0.04$. (d) Photoacoustic image at $880\mathrm{nm}$, $p_0(\mathbf{r}, 880\mathrm{nm})$.

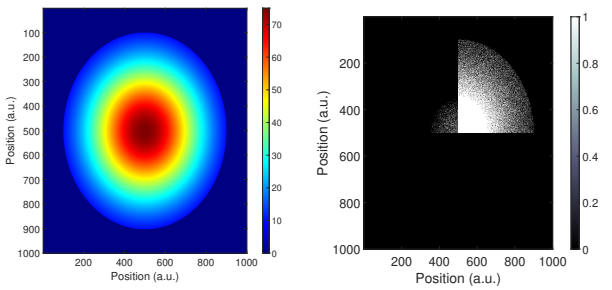

(a) (b)

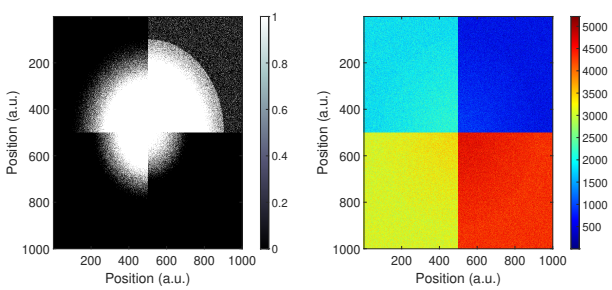

(c) (d)

Fig. 5: Detection of radially decreasing gold nanoparticles with regions of varying oxyhemoglobin and deoxyhemoglobin concentrations.(a) Concentration of gold nanoparticles, $C_{\mathrm{AuNP}}(\mathbf{r})$. (b) Detection of gold nanoparticles, $\Xi_{\mathrm{AuNP}}(\mathbf{r})$, with $K = 5$ and $T = 0.75$. (c) Detection of gold nanoparticles, $\Xi_{\mathrm{AuNP}}(\mathbf{r})$, with $K = 10$ and $T = 0.04$. (d) Photoacoustic image at $880\mathrm{nm}$, $p_0(\mathbf{r}, 880\mathrm{nm})$.

B. Comparison of the Least Squares Method and the Direct-Inverse Product Method Using Image Correlation

In this section, the performance of the Direct-Inverse Product Method is evaluated through three simulations conducted in MATLAB, resulting in two figures per simulation. In all simulations, three chromophores were considered: 1) oxyhemoglobin ($\mathrm{HbO_2}$), 2) deoxyhemoglobin (Hb), and 3) gold nanoparticles (AuNP) as the contrast agent.. Additionally, the concentration matrices from the previous section were reused for each simulation.

Figures 6 and 7 illustrate the first simulation, which involves elliptical masked regions with concentrations of gold nanoparticles. The second simulation, shown in Figures 8 and 9, examines radially decreasing distributions of gold nanoparticles. Finally, Figures 10 and 11 present the third simulation, where radially decreasing gold nanoparticles are combined with regions of varying oxyhemoglobin and deoxyhemoglobin concentrations, adding complexity to the analysis.

In each simulation, gold nanoparticles were detected using the Least Squares Method (as described in **??**) and the Direct-Inverse Product Method (as described in **??**). The iterations K were varied from 0 to 100 in steps of 2, while the threshold T ranged from 0 to 1 in increments of 0.001.

Figures 6, 8, and 10 display the correlation values between the image detecting gold nanoparticles using the Least Squares Method and the images generated by the Direct-Inverse Product Method for the various K and T values tested. The maximum correlation values obtained for each simulation are summarized in Table II.

TABLE II: Comparison of Results Obtained in Simulations

Parameter	**Sim. Fig. 6,7**	**Sim. Fig. 8,9**	**Sim. Fig. 10,11**
K (iterations)	6	14	2
T (threshold)	0.104	0.010	0.428
Maximum correlation	0.5766	0.7580	0.8077

Furthermore, Figures 7, 9, and 11 illustrate the following: (a) the actual location of the gold nanoparticles, (b) the detection using the Least Squares Method, and (c) the image with the highest correlation obtained using the Direct-Inverse Product Method. Additionally, for Fig. 11, a fourth image (d) has been included, representing the sum of the oxyhemoglobin and deoxyhemoglobin concentrations, which increase counterclockwise.

Regarding the first simulation, associated with Figures 6 and 7, the method's capability to detect regions with AuNP concentrations is demonstrated. The correlation values range from 0 to 0.5766, as shown in Fig. 6. As the number of iterations increases, the threshold T converges to approximately 0.3, represented by the green region in the heatmap.

Figure 7 highlights the differences between detection methods, where the Direct-Inverse Product Method introduces false positives and negatives. This behavior is attributed to repeated iterations, which amplify the discrepancies between pixels of higher and lower magnitudes. These discrepancies, while potentially limiting accuracy, underline the method's sensitivity to iterative adjustments and the need for parameter optimization in practical applications.

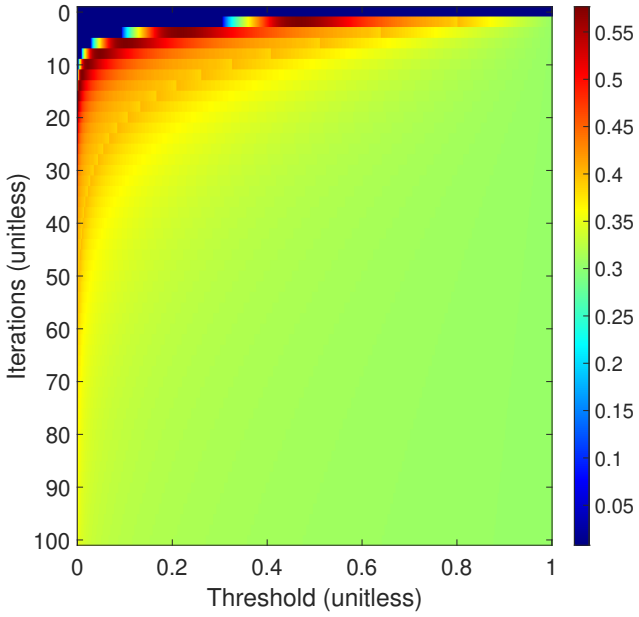

Fig. 6: Heatmap of the correlation as a function of iterations K and threshold T for the distribution of elliptical masks representing the concentration of gold nanoparticles, comparing images generated by the Least Squares Method and the Direct-Inverse Product Method.

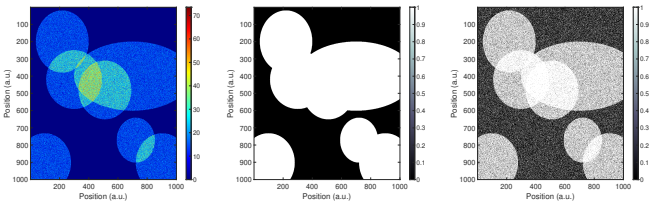

(a) (b) (c)

Fig. 7: Detection of elliptical masked regions containing concentrations of gold nanoparticles. (a) Gold nanoparticle concentration, $C_{\mathrm{AuNP}}(\mathbf{r})$. (b) Detection of gold nanoparticles using the Least Squares Method. (c) Maximum correlation image for the detection of gold nanoparticles using the Direct-Inverse Product Method with optimal iterations ($K = 6$) and optimal threshold ($T = 0.104$).

Similarly, in the simulation associated with Figures 8 and 9, the method's capability to detect regions with AuNP concentrations is demonstrated. The correlation values range from 0 to 0.7580, as shown in Fig. 8. As the number of iterations increases, the threshold T converges to approximately 0.5, represented by the orange region in the heatmap. This corresponds to the highest average correlation among the three simulations.

In Fig. 9, the differences between the methods are observed primarily at the circle's edge and its exterior. These results demonstrate the successful detection of all regions with higher concentrations, validating the method's effectiveness in handling radially decreasing distributions.

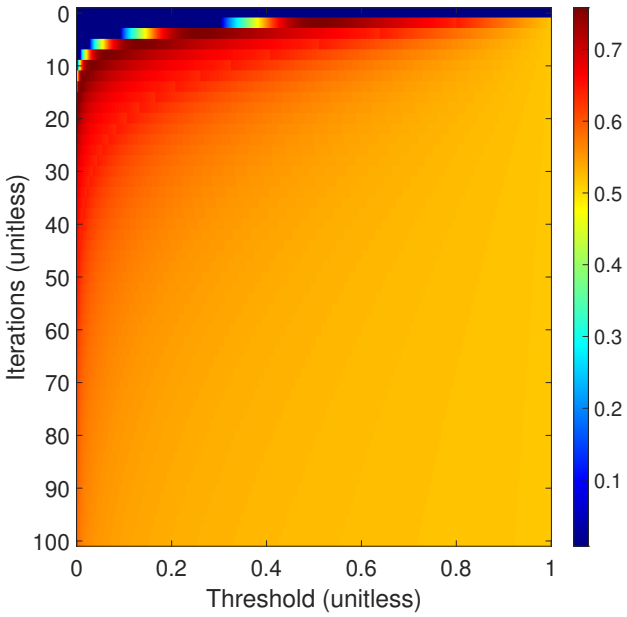

Fig. 8: Heatmap of the correlation as a function of iterations K and threshold T for the distribution of radially decreasing gold nanoparticles, comparing images generated by the Least Squares Method and the Direct-Inverse Product Method.

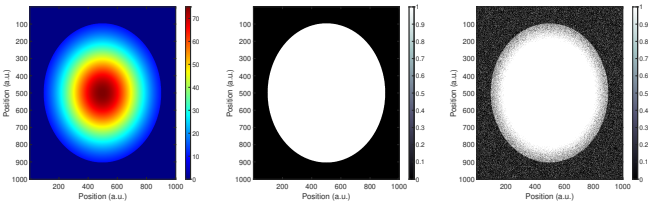

(a) (b) (c)

Fig. 9: Detection of radially decreasing gold nanoparticles. (a) Gold nanoparticle concentration, $C_{\mathrm{AuNP}}(\mathbf{r})$. (b) Detection of gold nanoparticles using the Least Squares Method. (c) Maximum correlation image for the detection of gold nanoparticles using the Direct-Inverse Product Method with optimal iterations ($K = 14$) and optimal threshold ($T = 0.7580$).

Finally, in the simulation associated with Figures 10 and 11, gold nanoparticles are successfully detected with correlation values ranging from 0 to 0.8077. This experiment achieves

the highest correlation value; however, the correlation also converges to the lowest average among the three experiments, approximately 0.2, as indicated by the light blue region in Fig. 10.

Figure 11 reveals that the Direct-Inverse Product Method introduces a higher number of false positives in the first quadrant, where the concentrations of oxyhemoglobin and deoxyhemoglobin are elevated. Interestingly, as these concentrations increase further, the number of false positives decreases, but this comes at the expense of introducing false negatives in other regions. This trade-off underscores the sensitivity of the Direct-Inverse Product Method to variations in chromophore concentrations and highlights the need for further parameter optimization in complex tissue environments.

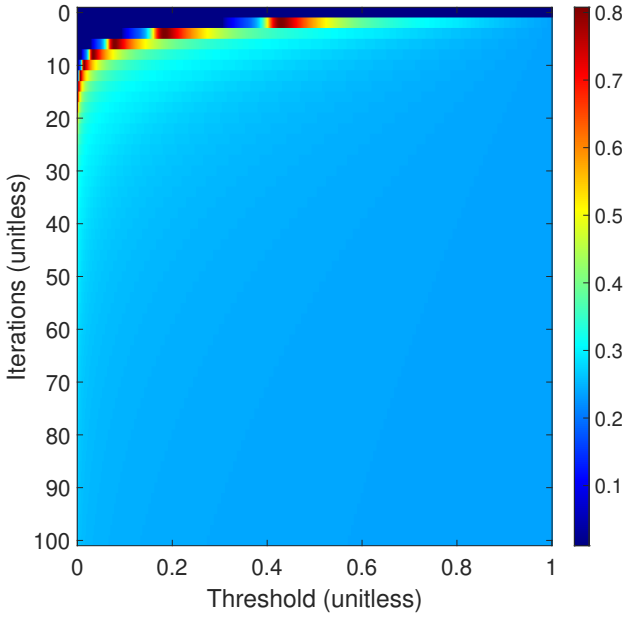

Fig. 10: Heatmap of the correlation as a function of iterations K and threshold T for the distribution of radially decreasing gold nanoparticles with regions of varying oxyhemoglobin and deoxyhemoglobin con- centrations, comparing images generated by the Least Squares Method and the Direct-Inverse Product Method.

IV. Conclusion

This study presented a comparative analysis of the Least Squares Method and the Direct-Inverse Product Method, the latter developed by the authors, for detecting gold nanoparticles (AuNPs) in photoacoustic imaging. Through three simulated scenarios, involving different chromophore distributions (oxyhemoglobin, deoxyhemoglobin, and AuNPs), the Direct-Inverse Product Method demonstrated its capability to achieve high correlation values using only two wavelengths. The highest correlation (0.8077) was achieved in the most complex scenario, highlighting the method's robustness in handling heterogeneous tissue environments.

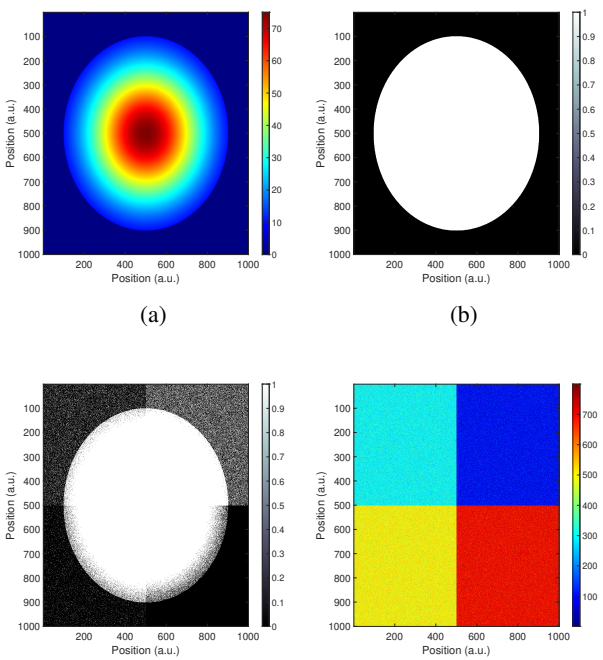

Fig. 11: Detection of radially decreasing gold nanoparticles with regions of varying oxyhemoglobin and deoxyhemoglobin con- centrations. (a) Gold nanoparticle concentration, $C_{\mathrm{AuNP}}(\mathbf{r})$. (b) Detection of gold nanoparticles using the Least Squares Method. (c) Maximum correlation image for the detection of gold nanoparticles using the Direct-Inverse Product Method with optimal iterations ($K = 0.2$) and optimal threshold ($T = 0.428$). (d) Concentrations of oxyhemoglobin and deoxyhemoglobin increasing counterclockwise.

The results underscore the importance of optimizing the parameters K and T, as they significantly influence the detection quality. Proper adjustment of these parameters enhances sensitivity, particularly in scenarios with low contrast agent concentrations. However, the method's reliance on the geometry of molar absorption curves limits its general applicability compared to the Least Squares Method, which remains robust across all tested conditions.

One of the primary limitations of this study is that the Direct-Inverse Product Method was validated only in controlled simulations. Experimental challenges such as noise, light scattering, and attenuation must be addressed to ensure its reliability in real-world applications. Furthermore, the method's iterative nature introduces false positives and negatives, particularly in regions with varying chromophore concentrations, emphasizing the need for further parameter tuning.

Despite these limitations, the Direct-Inverse Product Method offers a computationally simpler alternative to the Least Squares Method in scenarios with wavelength constraints. Table III provides a summary of the key differences between these methods, highlighting the trade-offs between computa-

tional simplicity and general applicability.

TABLE III: Comparison Between the Least Squares Method and the Direct-Inverse Product Method

Direct-Inverse Product Method	Least Squares Method
Requires only 2 wavelengths.	Requires at least $N+1$ wavelengths.
Does not require knowledge of the Grüeneisen coefficient or fluence.	Requires knowledge of the Grüeneisen coefficient and fluence.
Applicable only when the geometry of the molar absorption curves is appropriate.	Applicable under all conditions.
Based on an analysis of the geometry of molar absorption curves.	Based on linear regression.

Future work will focus on experimental validation and extending the method to scenarios where the properties defined in (19) and (20) are not satisfied. The potential for applications in areas such as cancer detection, where precise nanoparticle localization is critical, underscores the significance of further developing this approach.

Appendix A
Implications of the Chromophore's Physical Properties on Concentration

Consider a region of space with a volume V_T in m^3. Let n be an arbitrary chromophore, and let C_n represent its concentration in $\mathrm{mol}/\mathrm{m}^3$ within that volume. Then:

$$C_n = \frac{\eta_n}{V_T} \tag{34}$$

Where η_n represents the moles of n within V_T. Now, if n occupies a mass m_n in kg and a volume V_n in m^3 within V_T, the molar mass M_n in kg/mol and the density ρ_n in kg/m^3 are given by the following expressions:

$$M_n = \frac{m_n}{\eta_n} \tag{35}$$

$$\rho_n = \frac{m_n}{V_n} \tag{36}$$

By manipulating (35) and (36), equating the mass and solving for the moles, we can rewrite (34) as:

$$C_n = \frac{\rho_n}{M_n}\frac{V_n}{V_T} \tag{37}$$

Assume the physical properties of the gold nanoparticles are $\rho_{\mathrm{AuNP}} \approx 19300\mathrm{kg}/\mathrm{m}^3$ and $M_{\mathrm{AuNP}} \approx 0.197\mathrm{kg}/\mathrm{mol}$. Meanwhile, the molar mass of hemoglobin is $M_{\mathrm{HbO_2}} \approx M_{\mathrm{Hb}} \approx 64.5\mathrm{kg}/\mathrm{mol}$. Now, if we assume that the density of hemoglobin is approximately that of water, i.e., $\rho_{\mathrm{HbO_2}} \approx \rho_{\mathrm{Hb}} \approx 1000\mathrm{kg}/\mathrm{m}^3$ [14]. If both chromophores occupy a volume V within V_T, by substituting into (34):

$$C_{\mathrm{AuNP}} \approx (97969.54)\frac{V}{V_T} \tag{38}$$

$$C_{\mathrm{HbO_2}} \approx C_{\mathrm{Hb}} \approx (15.50)\frac{V}{V_T} \tag{39}$$

Note that these calculations demonstrate that gold nanoparticles are an excellent contrast agent not only because of their optical absorption properties but also because, within the same volume element, they can achieve concentrations up to 6300 times greater than that of hemoglobin. It is important to note from (2) that optical absorption is influenced not only by the specific absorption coefficients of each chromophore but also by their concentration and, consequently, by their physical properties.

References

[1] J. Wallyn, N. Anton, S. Akram *et al.*, "Biomedical imaging: Principles, technologies, clinical aspects, contrast agents, limitations and future trends in nanomedicines," *Pharmaceutical Research*, vol. 36, no. 7, p. 78, 2019. [Online]. Available: https://doi.org/10.1007/s11095-019-2608-5

[2] J. Weber, P. Beard, and S. Bohndiek, "Contrast agents for molecular photoacoustic imaging," *Nature Methods*, vol. 13, pp. 639–650, 2016. [Online]. Available: https://doi.org/10.1038/nmeth.3929

[3] R. Acharya, R. Wasserman, J. Stevens, and C. Hinojosa, "Biomedical imaging modalities: a tutorial," *Computerized Medical Imaging and Graphics*, vol. 19, no. 1, pp. 3–25, 1995. [Online]. Available: https://www.sciencedirect.com/science/article/pii/0895611194000433

[4] P. Beard, "Biomedical photoacoustic imaging," *Interface Focus*, vol. 1, no. 4, pp. 602–631, 2011. [Online]. Available: https://doi.org/10.1098/rsfs.2011.0028

[5] G. P. Luke, D. Yeager, and S. Y. Emelianov, "Biomedical applications of photoacoustic imaging with exogenous contrast agents," *Annals of biomedical engineering*, vol. 40, pp. 422–437, 2012.

[6] J. Yao and L. V. Wang, "Photoacoustic tomography: fundamentals, advances and prospects," *Contrast media & molecular imaging*, vol. 6, no. 5, pp. 332–345, 2011.

[7] C. L. Bayer, G. P. Luke, and S. Y. Emelianov, "Photoacoustic imaging for medical diagnostics," *Acoustics today*, vol. 8, no. 4, p. 15, 2012.

[8] D. Dumani, I.-C. Sun, and S. Emelianov, "In vivo photoacoustic detection of lymph node metastasis using glycol-chitosan-coated gold nanoparticles," in *2017 IEEE International Ultrasonics Symposium (IUS)*, 2017, pp. 1–4.

[9] B. T. Cox, S. R. Arridge, and P. C. Beard, "Estimating chromophore distributions from multiwavelength photoacoustic images," *Journal of the Optical Society of America A*, vol. 26, no. 3, pp. 443–455, 2009.

[10] K. T. Parra and D. D. Jarquín, "Algoritmo de clasificación de agentes de contraste exógenos usando imágenes de espectroscopía fotoacústica suave," *Ingeniería: Revista de la Universidad de Costa Rica*, vol. 33, no. 3, pp. 73–79, 2023.

[11] S. Kim, Y.-S. Chen, G. P. Luke, and S. Y. Emelianov, "In vivo three-dimensional spectroscopic photoacoustic imaging for monitoring nanoparticle delivery," *Biomedical optics express*, vol. 2, no. 9, pp. 2540–2550, 2011.

[12] H. A. Strobel, S. M. Moss, and J. B. Hoying, "Methods for vascularization and perfusion of tissue organoids," *Mammalian Genome*, vol. 33, no. 3, pp. 437–450, 2022.

[13] F. A. Amiri and J. Zhang, "Tissue oxygenation around capillaries: Effects of hematocrit and arteriole oxygen condition," *Bulletin of Mathematical Biology*, vol. 85, no. 6, p. 50, 2023.

[14] D. J. Vitello, R. M. Ripper, M. R. Fettiplace, G. L. Weinberg, and J. M. Vitello, "Blood density is nearly equal to water density: a validation study of the gravimetric method of measuring intraoperative blood loss," *Journal of veterinary medicine*, vol. 2015, no. 1, p. 152730, 2015.